Journal of Applied Physics

# Design of semiconductor surface pits for fabrication of regular arrays of quantum dots and nanorings

Cite as: J. Appl. Phys. **125**, 045303 (2019); https://doi.org/10.1063/1.5064807
Submitted: 08 October 2018 . Accepted: 12 January 2019 . Published Online: 30 January 2019

Ashish Kumar, Chao-Shou Chen, and Dimitrios Maroudas



AIP Publishing

Journal of Applied Physics | ARTICLE | scitation.org/journal/jap

# Design of semiconductor surface pits for fabrication of regular arrays of quantum dots and nanorings

Cite as: J. Appl. Phys. **125**, 045303 (2019); doi: 10.1063/1.5064807
Submitted: 8 October 2018 · Accepted: 12 January 2019 ·
Published Online: 30 January 2019

View Online Export Citation CrossMark

Ashish Kumar, Chao-Shou Chen, and Dimitrios Maroudas[a)]

## AFFILIATIONS

Department of Chemical Engineering, University of Massachusetts Amherst, Amherst, Massachusetts 01003-9303, USA

[a)]**Author to whom correspondence should be addressed:** maroudas@ecs.umass.edu

## ABSTRACT

We report a systematic computational study on the formation of complex nanostructures consisting of quantum dots and nanorings on surfaces of coherently strained thin films grown epitaxially on pit-patterned substrates. The analysis is based on self-consistent dynamical simulations according to a film surface evolution model that has been validated experimentally by comparison of its predictions with experimental observations on Ge films grown on Si pit-patterned substrates and is supported by linear stability theory that explains the film surface nanopattern formation as the outcome of a Stranski-Krastanow instability. Emphasis is placed on the design of conical pit patterns and the effects on the resulting film surface nanopattern of varying geometrical design parameters including film thickness, pit-pattern period, pit depth, pit opening diameter, and pit wall inclination. We demonstrate that varying the pit opening diameter and the pit wall slope leads to formation of complex nanostructures inside the pits of a regular pit pattern on the film surface, which include quantum dots, as well as single nanorings and multiple concentric nanorings that may or may not surround a central quantum dot inside each pit. Our simulation predictions demonstrate that the ordered nanostructure patterns forming on the film surface can be controlled precisely by tuning the geometrical parameters of the pits on the pit-patterned substrate. Our findings have important implications for designing optimal semiconductor surface patterns toward enabling future nanofabrication technologies.



## I. INTRODUCTION

Semiconductor quantum dots (QDs) and nanorings are material nanostructures that enable a broad range of technological applications, including electronic and photonic devices,[1–4] sensing,[5,6] as well as magnetic recording device technologies.[7] Stranski-Krastanow (SK) growth[8,9] is a common method of growing such nanostructures on surfaces of epitaxially deposited thin films driven by the induced biaxial stress in the epitaxial film because of its lattice mismatch with the substrate material. However, the formation of quantum dots as a result of SK growth instabilities leads to their random arrangement on the film surface lacking uniformity in their size and distribution. Such a random arrangement of nanostructures is not a desirable outcome for applications that typically require a uniform positioning and ordering of nanoscale features on a planar surface. Recent studies have explored various strategies for guiding the formation of regular patterns of uniformly sized nanostructures on surfaces of epitaxial films by pursuing the film's deposition on substrates with engineered morphologies.[10–14]

Epitaxial growth of coherently strained thin films on substrates with pit-patterned surfaces has been a successful approach for self-assembled ordered quantum dot pattern formation.[15–18] Semiconductor heteroepitaxial film/substrate systems where this method of formation of ordered nanostructures has been pursued successfully include Ge/Si,[15–17] InN/GaN,[18] InAs/GaAs,[19] and Ge/$Si_3N_4$.[20] Periodic patterns of one or more QDs on the surface of films grown epitaxially inside the pits[16,17,19] and nanoring-like structures forming at the rims of these pits[15,16,18,20] are among the ordered nanostructures that have been fabricated in the above experimental studies.

Surface morphological evolution of epitaxial thin films deposited on patterned substrates, including quantum dot formation on pit-patterned substrates, has been analyzed in theoretical and computational studies using continuum-scale models and Monte Carlo simulations.[21–25] The morphology of a pit that forms on the surface of an epitaxial film grown on a pit-patterned substrate has been analyzed in Ref. 21 based on a phase field model. Asymptotic states of QD patterns on the epitaxial film surface have been predicted in analyses of morphological stability and simulations of morphological evolution of epitaxial film surfaces perturbed from a planar state according to plane-wave patterns.[22,23] Strained island nucleation on patterned substrates has been studied based on analytical thermodynamic models,[24] and Monte Carlo simulations have demonstrated Ge island self-assembly and ordering mechanisms on pre-patterned Si{001} substrates.[25] In a recent study, we developed a continuous-domain kinetic model of epitaxial film surface morphological response for coherently strained films on pit-patterned semiconductor substrates.[26] We used this model to interpret experimental results of ordered quantum dot pattern formation on surfaces of Ge films grown epitaxially on pit-patterned Si substrates, with quantum dots emerging inside the pits and nanorings forming at the rims of the pits.[16,17] However, in spite of these earlier studies, the effects of systematically varying the numerous pit pattern design parameters on the resulting epitaxial film surface nanostructure pattern remain unexplored.

In the present study, we use our experimentally validated kinetic model of surface morphological response of epitaxial films on pit-patterned substrates to explore the effects on film surface nanopattern formation of varying the geometrical design parameters of the pit pattern. We focus on conical pit geometries and examine the effects of five key parameters: film thickness, pit-pattern period, pit depth, pit opening diameter, and pit wall slope. We find that the pit opening diameter and the pit wall slope are particularly important design parameters and their proper tuning can lead to formation of patterns of nanostructures, such as quantum dots and nanorings inside the pits. The complexity of the nanostructures forming inside the pits can be increased with increasing pit opening diameter or making the pit wall slope steeper; such nanostructures include single nanorings or multiple concentric nanorings that may or may not surround a central QD. The formation of all of these nanoscale features inside pits on the film surface is explained by linear stability theory (LST) as outcomes of an SK instability undergone by the epitaxial film.

The rest of the article is structured as follows. The model of surface morphological evolution of a coherently strained epitaxial film on a pit-patterned substrate is described in Sec. II. Our simulation results for the film surface morphological response are presented and discussed in Sec. III, where the effects of varying the geometrical design parameters of the pits in the pit pattern, namely, the pit-pattern period, the film thickness, the pit depth, the size of the pit opening, and the pit wall inclination, are examined separately and systematically. Our simulation findings on the nanoscale features of the regular nanopattern forming on the film surface as a result of the film's surface morphological response are explained in Sec. IV based on linear stability theory. Finally, the main conclusions of our study are summarized in Sec. V.

## II. SURFACE EVOLUTION MODEL

For the analysis of the deposited film surface morphological evolution, we consider a coherently strained thin film grown epitaxially on a thick substrate with the film surface morphology shown in Fig. 1(a) as the initial configuration. This film surface configuration is further highlighted in Figs. 1(b) and 1(c) and mimics that of the surface of a film deposited through layer-by-layer growth on a pit-patterned substrate surface such as the films deposited in the experiments of Refs. 16 and 17. In our analysis, the initial configuration consists of a thin film the surface of which is located at a distance $h_0$ above the surface of the substrate on which the film is deposited, as depicted in Fig. 1(d); i.e., our analysis of the film surface morphological response at the temperature of the deposition experiments[15–20] does not correspond to a direct simulation of the epitaxial film growth from zero thickness to its final thickness, $h_0$. In other words, in our model, the film's initial configuration takes the shape of the regular pit pattern on the substrate surface with the pits repeated periodically on the film's surface as shown in the regular array (square lattice) of surface pits of Fig. 1; all the

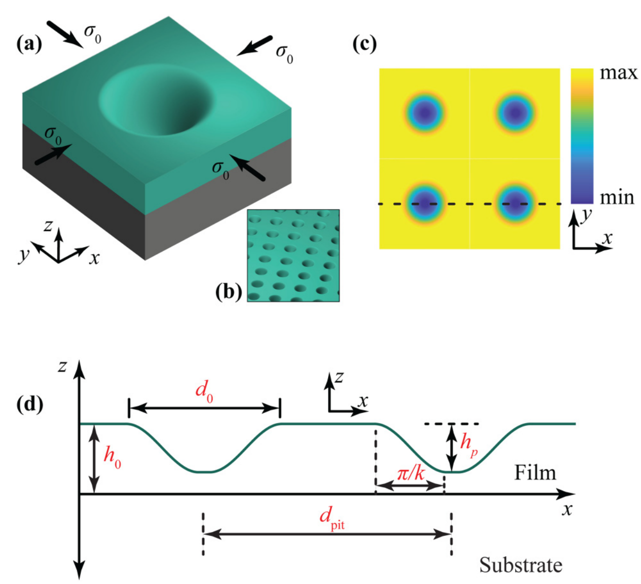


**FIG. 1.** Schematic representation of (a) a unit cell of the initial configuration of a periodic pattern of pits shown in (b) on the surface of a coherently strained thin film. The initial pit pattern on the film surface mimics the shape of the pit-patterned substrate, consisting of a regular array of pits in the shape of inverted truncated cones. (c) 2D contour map of surface morphology, $h(x, y)$, of four ($2 \times 2$) such unit cells. (d) 1D surface profile of the configuration in (c) along the dashed black line on the 2D contour map.

geometrical parameters required for a complete design of such a pit pattern are listed in Fig. 1(d) and include, in addition to the film thickness, the pit depth, the pit opening size, the pit wall inclination, and the center-to-center distance between neighboring pits. In this study, we focus on pits with a shape that resembles an inverted truncated cone with a circular base and a circular pit opening: we term such pit configurations as "conical" pits. The wall of the pit is represented by half a wavelength of a cosinusoidal wave with wave number $k$; the pit wall slope is controlled by tuning $k$ and increasing $k$ results in pit walls with steeper inclination.

The coherently strained (due to lattice mismatch with the substrate) epitaxial film is subject to an equibiaxial stress of magnitude $\sigma_0$ with nonzero stress components in the $x$- and $y$-directions of a Cartesian frame of reference as shown in Fig. 1(a). We use the surface height function $h(x, y, t)$ for the parameterization of the film surface morphology. We express the film surface atomic flux using a Nernst-Einstein equation according to classical phenomenology and formulate the corresponding continuity equation for the expression of mass conservation, which gives the surface height evolution equation

$$\frac{\partial h}{\partial t} = H' \nabla_s \cdot \left[ \frac{\delta_s \Omega D_s}{k_B T} \nabla_s \left( U_E - \gamma_f \kappa + U_W \right) \right]. \tag{1}$$

In Eq. (1), $H' \equiv \{1 + (\partial h/\partial x)^2 + (\partial h/\partial y)^2\}^{1/2}$, $\Omega$ is the atomic volume, $\delta_s/\Omega$ expresses the number of surface atoms per unit area, $k_B$ is the Boltzmann constant, $T$ is the temperature, $D_s$ is the film surface atomic diffusivity, and $\nabla_s$ denotes the surface gradient operator. In the right-hand side of Eq. (1), within the bracketed flux expression, $\nabla_s$ acts on the chemical potential of the film surface atoms; this chemical potential includes contributions from the elastic strain energy, the surface energy, and the film's wetting potential, the densities of which are expressed by $U_E$, $\gamma_f \kappa$, where $\kappa$ is the surface curvature, and $U_W$, respectively. According to the "transition-layer" model,[27,28] the wetting potential density is given by

$$U_W = \frac{(\gamma_f - \gamma_s) b}{H' \pi (b^2 + h^2)}, \tag{2}$$

where $\gamma_f$ and $\gamma_s$ are the surface free energies per unit area of the film and substrate materials, respectively, and $b$ is the thickness of the transition layer. For simplicity, we neglect both the surface diffusivity and the surface free energy anisotropies; i.e., there is no surface orientation dependence specified for $D_s$ or $\gamma_f$; this assumption has no qualitative effects on the modeling predictions but only affects geometrical details (edge sharpness) of the nanoscale features that emerge from the film surface. For the computation of $U_E$, the elastostatic boundary-value problem (BVP) in the film is solved self-consistently with the evolution of the film surface, which is the moving boundary for this BVP, and the stress and strain tensors are evaluated at every point on the film surface. $U_E$ is calculated asymptotically, as described in detail in Ref. 29, based on regular perturbation theory and keeping up to second-order terms in the asymptotic expansion. In the calculations of the elastic strain energy of the thin film, the bulk value of the elastic modulus of the thin film is used. With Ge/Si considered as a prototypical heteroepitaxial system for the analysis, this is a satisfactory assumption: for a Ge/Si film/substrate system on a practically infinitely thick Si substrate and for the lattice mismatch characteristic of this heteroepitaxial material system, we do not expect the elastic properties of Ge to be substantially different from their bulk values and that any such differences have any effect on the findings of this study.

The characteristic length and time scales of the problem under consideration, $l$ and $\tau$, respectively, are estimated by the dimensional analysis of Eq. (1), which gives $l = M_s \gamma_f / \sigma_0^2$ and $\tau = k_B T l^4 / [\delta_s \Omega D_s \gamma_f]$; in the above expressions, $M_s$ is the biaxial modulus of the substrate and $\sigma_0$ is the magnitude of the biaxial stress in a reference-state configuration of the film with planar film surface morphology. The dimensional analysis also yields the dimensionless parameter $\Xi_W = [2b(\gamma_s - \gamma_f)/(\pi h_0^3 \gamma_f)] l^2$, which expresses the strength of the wetting potential.[29] For the prototypical system of a Ge film on a Si substrate at 700°C, the estimated values of $l$ and $\tau$ are $l \approx 17$ nm and $\tau \approx 8.1$ min $\approx 485$ s. We have validated the above model by comparing the results of numerical simulations for the surface evolution of a Ge film deposited on a pit-patterned Si substrate according to this model with the experimental results of Ref. 17.[26] Specifically, in Ref. 26, we have reported detailed quantitative comparisons between experimental findings for epitaxially grown Ge thin films on pit-patterned Si{100} substrates and the corresponding simulation results based on our film surface evolution model. Those systematic comparisons highlight that the simulations are able to reproduce the nanostructures formed on the film surface in the experiments as well as their main features.

## III. SIMULATION RESULTS AND DISCUSSION

We have conducted a systematic protocol of self-consistent dynamical simulations according to the surface evolution model of Sec. II in order to explore the film surface morphological dynamics for the film with the pattern of conical pits shown in Fig. 1 and investigate the effects of varying the several pit design parameters on the film surface dynamical response. In the simulations, we solve the elastostatic BVP self-consistently with the propagation of the film surface as described in Ref. 29. Our numerical implementation of the surface evolution model is based on a spectral collocation method,[28] where the film surface is discretized using $512 \times 512$ grid points and discrete fast Fourier transforms are carried out. For monitoring the evolving surface morphology, we integrate Eq. (1) employing an advanced operator splitting-based semi-implicit spectral method[30] with adaptive time step size. In the simulations, the film thickness $h_0$ is always taken to be well above the critical film thickness required for triggering the SK morphological instability; this critical thickness is approximately equal to 3 monolayers for Ge/Si{100}.[8,31,32]

The surface morphology that evolves under the action of the driving forces that contribute to the chemical potential gradient of Eq. (1), from its initial configuration, can reach a sequence of asymptotic states over time. We can use the RMS roughness[33,34] of the film surface, SR, as a morphological metric to track these asymptotic states [the condition we pose for an asymptotic state to be realized in our dynamical simulations is $d(\mathrm{SR})/dt = d^2(\mathrm{SR})/dt^2 = 0$]. In Fig. 2, we show representative simulation results for the film surface morphological evolution in the case where the system reaches two asymptotic states, the first of which is reached over a faster time scale than the characteristic one for reaching the second. Figures 2(a1)–2(a4) show 2D contour maps of the surface morphology within the unit cell of a periodic pit pattern configuration on the film surface with the initial configuration depicted in Fig. 2(a1). Figures 2(b1)–2(b4) show the corresponding surface profiles of the configurations of Figs. 2(a1)–2(a4), along the $x$-direction of a cross section of the film perpendicular to the $xy$-plane and passing through the center of the unit cell. Figures 2(c1) and 2(c2) show the evolution of the film surface RMS roughness $SR(t)$ and its time derivative $d(\mathrm{SR})/dt$, respectively. The evolving surface morphology reaches its first asymptotic state over a time scale on the order of $1\,\tau$. For the case shown in Fig. 2, the heteroepitaxial system remains in the first asymptotic state until around $t = 2.0\,\tau$, with the "end" of this asymptotic state being marked by a downward pointing arrow in Fig. 2(c1). Over a longer time scale ($t > 9\,\tau$ in the case of Fig. 2), the system reaches another asymptotic state that is characterized by formation of multiple concentric nanorings on the film outside of the original pit region, Fig. 2(a4), with the formation of a central quantum dot inside the pit; in this case, the formation of this central QD is guaranteed (as we will see below) because of the proper choice of parameters such as the pit opening diameter and pit wall inclination. The nanoring formation on the rest of the film happens ultimately due to the SK instability being triggered and the propagation of the instability directed radially outwards by the presence of the pits; i.e., in this case, the nanoring forming at the rim of the original pit is the first nanoring formed. The instability then propagates radially outwards, resulting in sequential formation of each one of the concentric nanorings present in the longer-term asymptotic state. The time instant when each one of these concentric nanorings is formed is indicated by each one of the spikes in the $d(\mathrm{SR})/dt$ evolution plot shown in Fig. 2(c2). These nanorings resemble the nanoring configurations that have been demonstrated in a recent study to form due to thermal stress development upon thermal annealing of stressed deposited thin films as a result of a morphological transformation of larger quantum dots already present in the film prior to the thermal annealing.[35] The concentric nanorings shown in Fig. 2(a4) are actually a metastable state as well and over longer time periods break up into many smaller-sized quantum dots. These QDs formed from the dissociation of these nanorings then rearrange themselves into a regular hexagonal lattice arrangement of smaller, uniformly sized QDs. Interesting physical phenomena that have been observed experimentally,[16,17] such as formation of quantum dots inside the pits and nanorings at the rims of the pits due to pattern formation during epitaxial film growth and/or subsequent annealing, constitute the first asymptotic state in the morphological evolution of the epitaxial film surface. Although these asymptotic states may

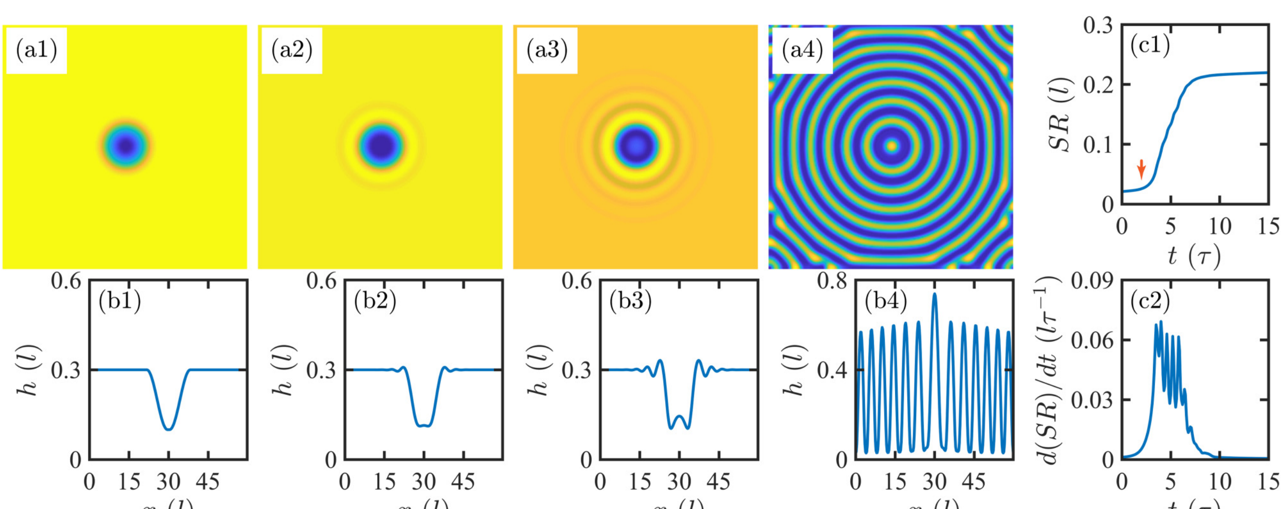


**FIG. 2.** (a) Representative 2D contour maps of simulated evolving surface morphology, $h(x, y, t)$, of a coherently strained thin film starting with a surface morphology that consists of a periodic arrangement of nanopits, with the top view of one such nanopit structure shown in the unit cell of the regular nanopit pattern for a conical pit at (a1) $t = 0$, (a2) $t = 1.0\,\tau$, (a3) $t = 2.0\,\tau$, and (a4) $t = 15.0\,\tau$. 1D surface profiles, $h(x; y, t)$, along the $x$-direction and passing through the center of the pit in the configurations of (a1), (a2), (a3), and (a4) are plotted in (b1), (b2), (b3), and (b4), respectively. The corresponding simulated evolution of the film surface RMS roughness, $SR(t)$, and its time derivative over a time period of $15\,\tau$ are plotted in (c1) and (c2), respectively, with the end of the first asymptotic state reached at a time marked by a downward pointing red arrow in (c1). The parameter values in the simulation are $d_0 = 16.5\,l$, $h_0 = 0.3\,l$, $d_{\mathrm{pit}} = 60\,l$, $h_p = 0.2\,l$, $k = 0.4\,l^{-1}$, and $\Xi_W = 0.0369$.

be metastable, kinetically trapped states, they are diffusionally driven and can be easily realized through diminishing the diffusion rates by lowering the temperature of the experiment and "freezing" the desired pattern in place.

Our study focuses on the film surface patterns that may form at this first asymptotic state inside the pits of the initial film surface morphology and how these patterns can be controlled by tuning the design parameters of the pit-patterned heteroepitaxial system. Instead of deposition processing or material parameters, we emphasize on the five key geometrical parameters of the pits in the regular pattern, as shown schematically in Fig. 1(d), namely, the pit-pattern period $d_{\mathrm{pit}}$, the epitaxial film thickness $h_0$, the pit depth $h_p$, the pit opening diameter $d_0$, and the pit wall slope controlled by the wave number $k$. In the rest of this section, we analyze and discuss the effects of each one of these geometrical parameters on the film surface pattern formed at the first asymptotic state.

### A. Effect of the pit-pattern period on film surface pattern

Figure 3 shows representative simulation results that capture the effect on the epitaxial film surface morphology of varying over a broad range the pit-pattern size $d_{\mathrm{pit}}$, i.e., the center-to-center distance between neighboring pits, emphasizing on the resulting nanopattern at the end of the first asymptotic state. Figures 3(a1)–3(a4), 3(b1)–3(b4), and 3(c1)–3(c4) show 2D contour maps of the evolving film surface morphology within the unit cell of a periodic pit pattern with the initial configurations of the film surface shown in Figs. 3(a1), 3(b1), and 3(c1), respectively. In these configurations, we increase $d_{\mathrm{pit}}$ from $36\,l$ to $60\,l$ while keeping all the other design parameters constant. Figures 3(a4), 3(b4), and 3(c4) show the 2D contour maps of the resulting film surface configurations at the end of the first asymptotic state, the 3D views of which are shown in Figs. 3(a5), 3(b5), and 3(c5), respectively. It is evident from these simulation results that varying the pit-pattern size has no qualitative effect on the resulting film surface nanopattern formation, i.e., $d_{\mathrm{pit}}$ variation does not cause any qualitative change in the film surface morphological response, as shown in the surface profiles of Figs. 3(a6), 3(b6), and 3(c6): all of these views and profiles of the film surface indicate that in all cases, regardless of the pit-pattern size, a single QD is formed at the center of each pit on the film's surface. This result from our simulations agrees with the results from the experimental studies of Ref. 17, which

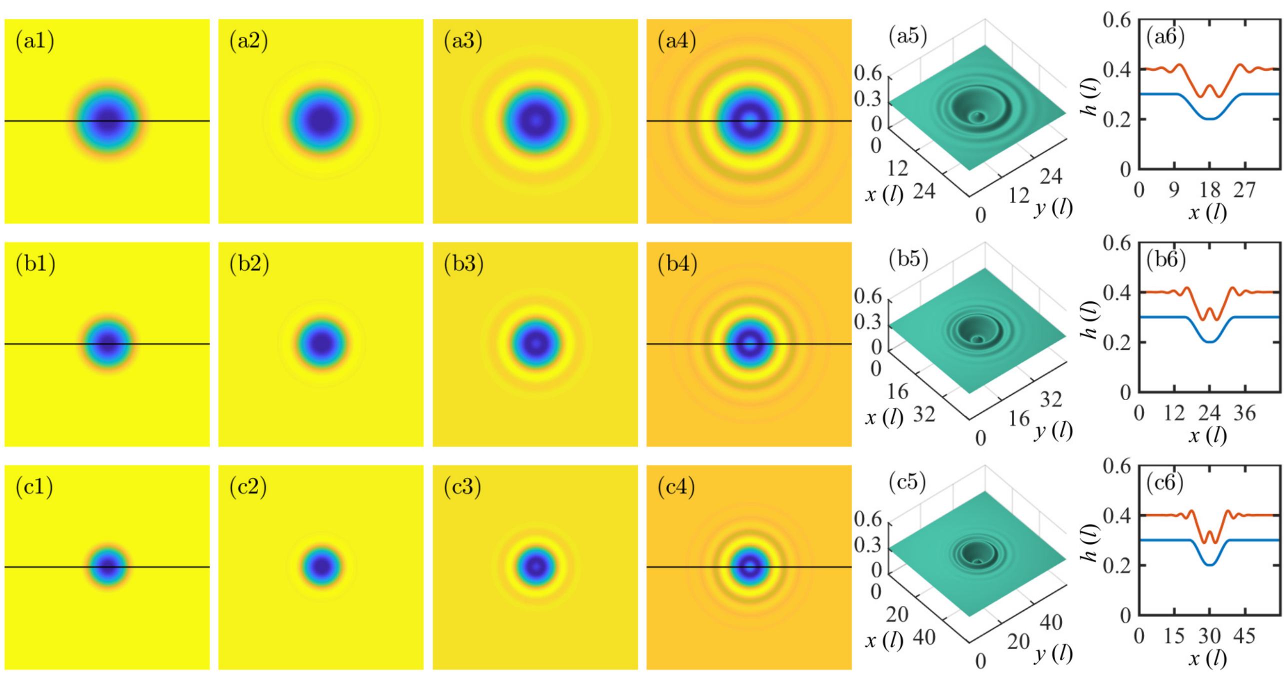


**FIG. 3.** (a)–(c) 2D contour maps of simulated evolving surface morphology, $h(x, y, t)$, of a coherently strained thin film starting with a surface morphology that consists of a periodic arrangement of nanopits, with the top view of one such nanopit structure shown in the unit cell of the regular nanopit pattern for a conical pit with pit-pattern period $d_{\mathrm{pit}}$ of (a1-a5) $36\,l$, (b1-b5) $48\,l$, and (c1-c5) $60\,l$ at (a1, b1, c1) $t = 0$, (a2, b2, c2) $t = 0.6\,\tau$, (a3, b3, c3) $t = 1.3\,\tau$, and (a4, b4, c4) $t = 2.0\,\tau$. 3D views of the film surface morphology corresponding to the top views shown in (a4), (b4), and (c4) are depicted in (a5), (b5), and (c5), respectively. 1D surface profiles, $h(x; y, t)$, along the black solid lines marked on the 2D contour maps of (a1) and (a4), (b1) and (b4), and (c1) and (c4) are plotted in blue and red, respectively, in (a6), (b6), and (c6), respectively. The 1D surface profiles plotted in red have been displaced upwards (along the $h$-axis) by $0.1\,l$ for clarity regarding their shapes. The other parameter values in the simulations are $h_0 = 0.3\,l$, $d_0 = 17\,l$, $h_p = 0.1\,l$, $k = 0.4\,l^{-1}$, and $\Xi_W = 0.0369$.

established that varying pit-pattern size over one order of magnitude has no effect on the resulting epitaxial film surface nanopattern. This agreement between our simulation predictions and such experimental data provides further validation for our film surface morphological evolution model of Sec. II.

### B. Effect of epitaxial film thickness on film surface pattern

Figure 4 shows representative simulation results that capture the effect of varying the epitaxial film thickness $h_0$ on the resulting film surface nanopattern at the end of the first asymptotic state. Figures 4(a1)–4(a4), 4(b1)–4(b4), and 4(c1)–4(c4) show 2D contour maps of the evolving film surface morphology within the unit cell of a periodic pit pattern with the initial film surface configurations shown in Figs. 4(a1), 4(b1), and 4(c1), respectively. In these heteroepitaxial system configurations, we increase $h_0$ from $0.3l$ to $0.9l$ while keeping all the other design parameters constant. Figures 4(a4), 4(b4), and 4(c4) show the 2D contour maps of the resulting film surface configurations at the end of the first asymptotic state; the 3D views of these film surface morphologies are shown in Figs. 4(a5), 4(b5), and 4(c5), respectively. These simulation results demonstrate that varying the film thickness over a broad range of $h_0$ does not have any qualitative effect on the resulting nanopattern formation as can be seen in the surface profiles of Figs. 4(a6), 4(b6), and 4(c6): regardless of film thickness, the resulting film surface nanopattern does not change and consists of a single QD occupying the central region of each pit in all cases. However, the quantitative effect of varying $h_0$ can be significant: increasing the epitaxial film thickness increases the accumulated elastic strain energy in the film, which leads to formation of more pronounced surface features as compared to those formed on the surface of a thinner film, namely, larger QDs and taller nanoring rims.

### C. Effect of pit depth on film surface pattern

Figure 5 shows representative simulation results that capture the effect of varying the pit depth $h_p$ on the resulting film surface nanopattern at the end of the first asymptotic state. Figures 5(a1)–5(a4), 5(b1)–5(b4), and 5(c1)–5(c4) show 2D contour maps of the evolving film surface shape within the unit cell of a periodic pit pattern with the initial epitaxial film surface configurations shown in Figs. 5(a1), 5(b1), and 5(c1),

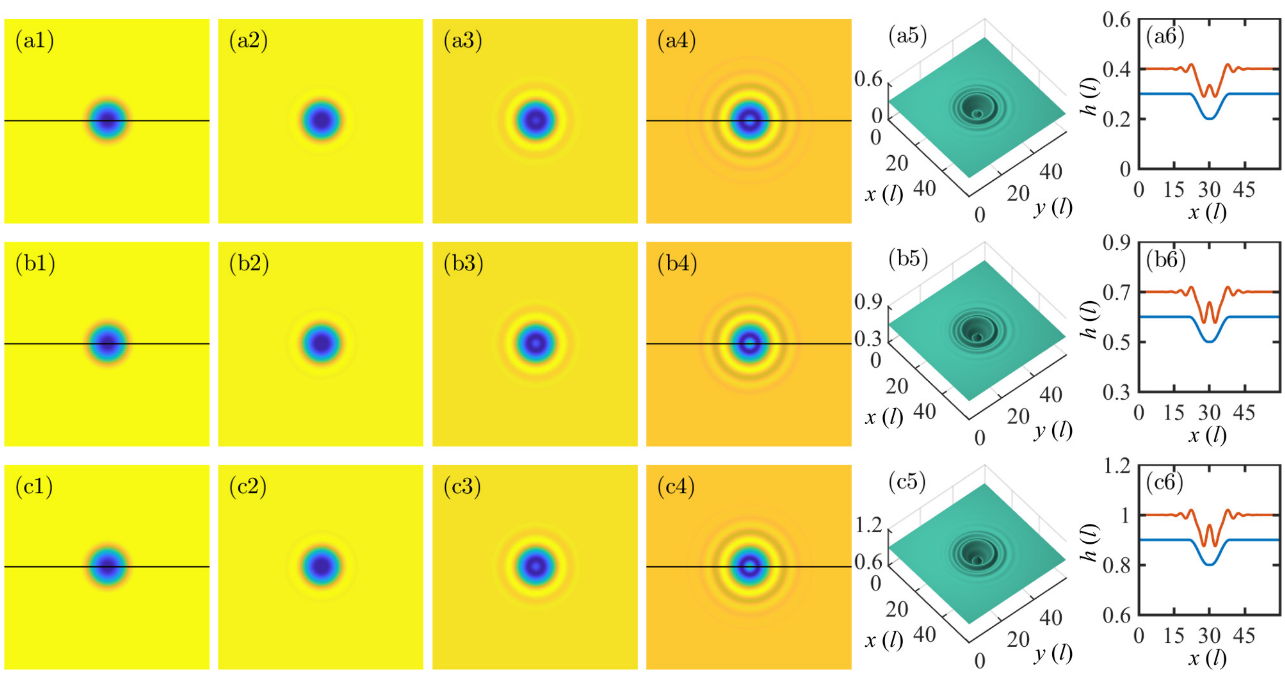


**FIG. 4.** (a)–(c) 2D contour maps of simulated evolving surface morphology, $h(x, y, t)$, of a coherently strained thin film starting with a surface morphology that consists of a periodic arrangement of nanopits, with the top view of one such nanopit structure shown in the unit cell of the regular nanopit pattern for a conical pit with deposited film thickness $h_0$ of (a1-a5) $0.3\,l$, (b1-b5) $0.6\,l$, and (c1-c5) $0.9\,l$ at (a1, b1, c1) $t = 0$, (a2, b2, c2) $t = 0.6\,\tau$, (a3, b3, c3) $t = 1.3\,\tau$, and (a4, b4, c4) $t = 2.0\,\tau$. 3D views of the film surface morphology corresponding to the top views shown in (a4), (b4), and (c4) are depicted in (a5), (b5), and (c5), respectively. 1D surface profiles, $h(x; y, t)$, along the black solid lines marked on the 2D contour maps of (a1) and (a4), (b1) and (b4), and (c1) and (c4) are plotted in blue and red, respectively, in (a6), (b6), and (c6), respectively. The 1D surface profiles plotted in red have been displaced upwards (along the $h$-axis) by $0.1\,l$ for clarity regarding their shapes. The other parameter values in the simulations are $d_{pit} = 60\,l$, $d_0 = 17\,l$, $h_p = 0.1\,l$, $k = 0.4\,l^{-1}$, and (a) $\Xi_W = 0.0369$, (b) $\Xi_W = 0.0046$, and (c) $\Xi_W = 0.0014$.

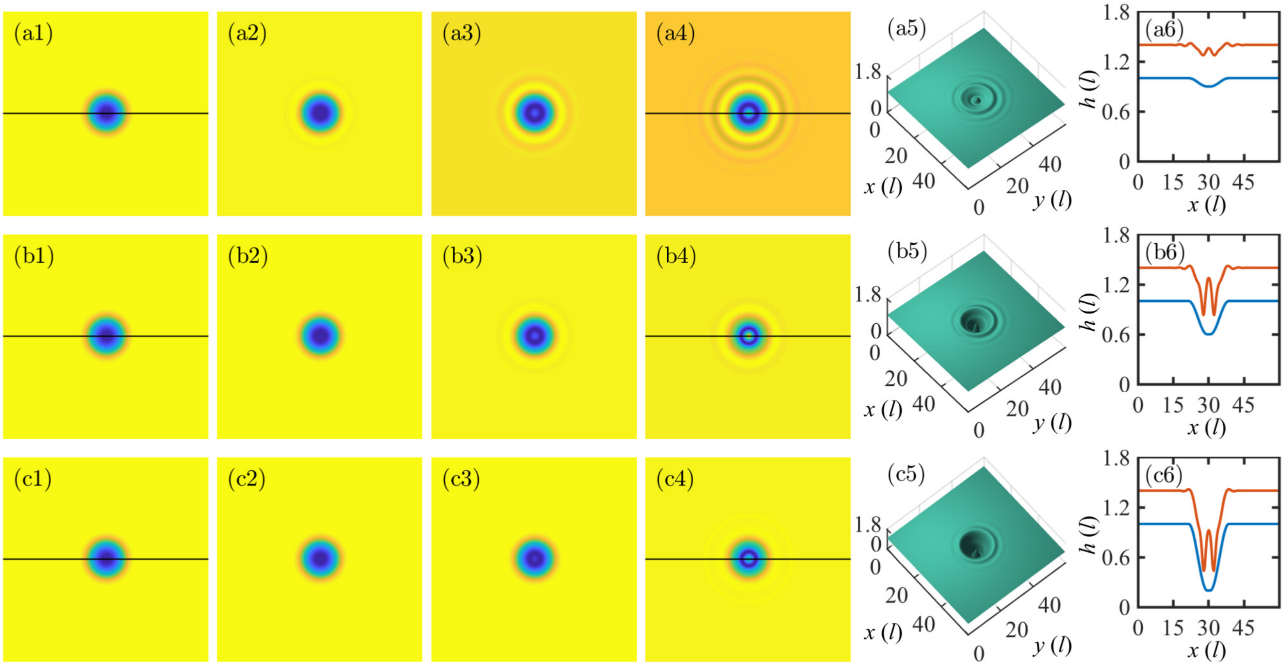


**FIG. 5.** (a)–(c) 2D contour maps of simulated evolving surface morphology, $h(x, y, t)$, of a coherently strained thin film starting with a surface morphology that consists of a periodic arrangement of nanopits, with the top view of one such nanopit structure shown in the unit cell of the regular nanopit pattern for (a1-a5) a conical pit with pit depth $h_p = 0.1\,l$ at (a1) $t = 0$, (a2) $t = 0.6\,\tau$, (a3) $t = 1.3\,\tau$, and (a4) $t = 2.0\,\tau$; (b1-b5) a conical pit with $h_p = 0.4\,l$ at (b1) $t = 0$, (b2) $t = 0.3\,\tau$, (b3) $t = 0.7\,\tau$, and (b4) $t = 1.2\,\tau$; and (c1-c5) a conical pit with $h_p = 0.8\,l$ at (c1) $t = 0$, (c2) $t = 0.1\,\tau$, (c3) $t = 0.3\,\tau$, and (c4) $t = 0.6\,\tau$. 3D views of the film surface morphology corresponding to the top views shown in (a4), (b4), and (c4) are depicted in (a5), (b5), and (c5), respectively. 1D surface profiles, $h(x; y, t)$, along the black solid lines marked on the 2D contour maps of (a1) and (a4), (b1) and (b4), and (c1) and (c4) are plotted in blue and red, respectively, in (a6), (b6), and (c6), respectively. The 1D surface profiles plotted in red have been displaced upwards (along the $h$-axis) by $0.4\,l$ for clarity regarding their shapes. The other parameter values in the simulations are $h_0 = l$, $d_0 = 17\,l$, $d_{\text{pit}} = 60\,l$, $k = 0.4\,l^{-1}$, and $\Xi_W = 9.95 \times 10^{-4}$.

respectively. In these heteroepitaxial configurations, we increase $h_p$ over a broad range, from $0.1l$ to $0.8\,l$, while keeping all the other system design parameters constant. Figures 5(a4), 5(b4), and 5(c4) show the 2D contour maps of the resulting film surface configurations at the end of the first asymptotic state, with the 3D views of the surface morphologies shown in Figs. 5(a5), 5(b5), and 5(c5), respectively. It is evident from these simulation results that varying the pit depth does not have any qualitative effect on the resulting nanopattern formation as shown in the surface profiles of Figs. 5(a6), 5(b6), and 5(c6). However, there is a quantitative effect of increasing the pit depth due to the increase in the thermodynamic driving force associated with the film surface curvature. As a result, the end of the first asymptotic state is reached earlier for film surfaces with deeper pits. Moreover, the ratio of the surface feature size formed inside the pit over the nanoring size formed at the rim of the pit increases with increasing pit depth. Therefore, the pit depth is a parameter that can be tuned to control the size (height and width) of the nanoring forming at the rim of the pits as opposed to controlling the nanoscale features that are formed inside the pits.

### D. Effect of the pit opening diameter on film surface pattern

Figure 6 shows representative simulation results that capture the effect of varying the pit opening diameter $d_0$ on the resulting film surface nanopattern at the end of the first asymptotic state. Figures 6(a1)–6(a4), 6(b1)–6(b4), 6(c1)–6(c4), and 6(d1)–(d4) show 2D contour maps of the evolving film surface morphology within the unit cell of a periodic pit pattern with the initial epitaxial film surface configurations shown in Figs. 6(a1), 6(b1), 6(c1), and 6(d1), respectively. In these heteroepitaxial configurations, we vary $d_0$ over a broad range while keeping all other parameters constant. Figures 6(a4), 6(b4), 6(c4), and 6(d4) show the 2D contour maps of the resulting film surface configurations at the end of the first asymptotic state, with the 3D views of these film surface morphologies depicted in Figs. 6(a5), 6(b5), 6(c5), and 6(d5), respectively. These simulation results demonstrate clearly that varying the pit opening diameter has a significant qualitative effect on the resulting nanopattern formation as can be seen in the surface profiles of Figs. 6(a6), 6(b6), 6(c6), and 6(d6). Our simulations predict that the surface morphological evolution of an epitaxial film deposited on a conical pit with a pit

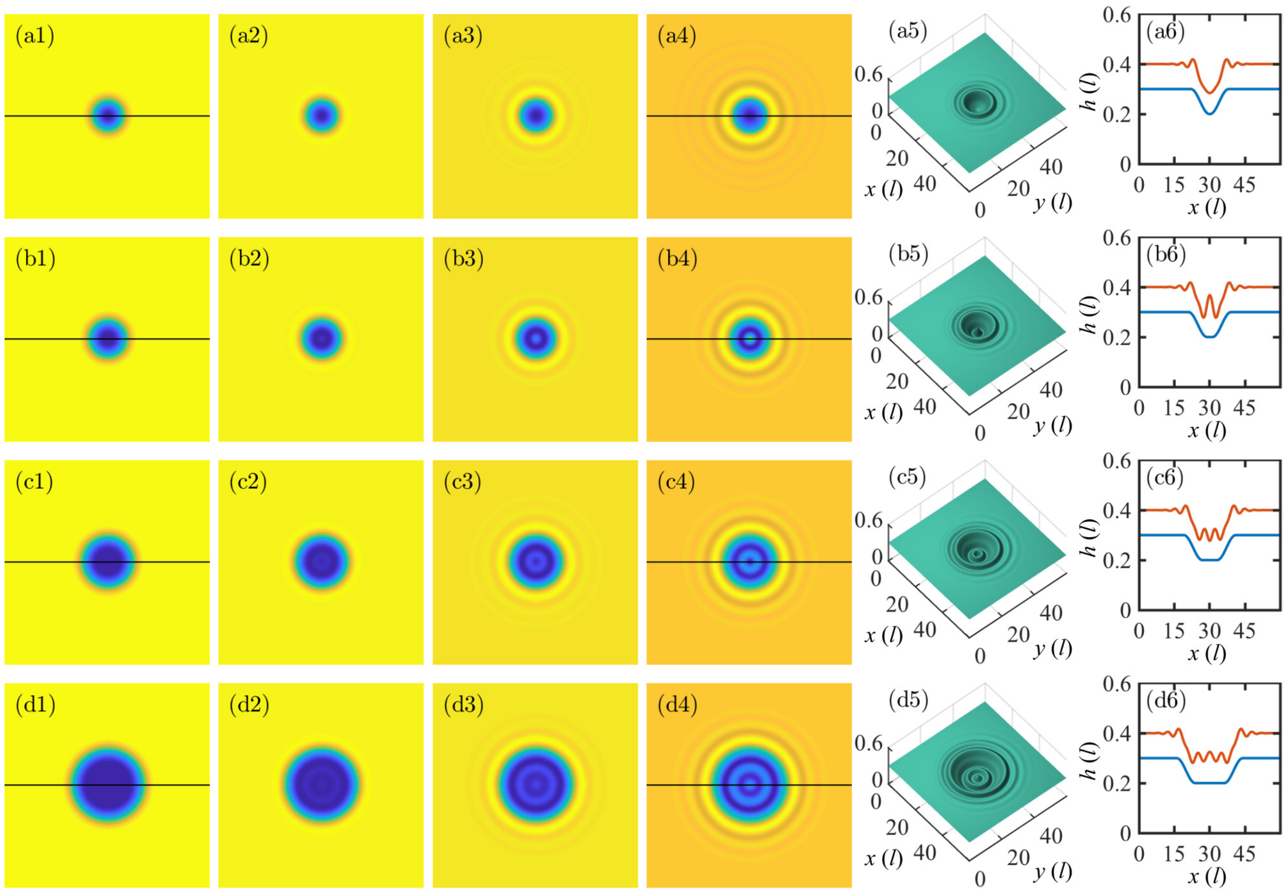


**FIG. 6.** (a)–(d) 2D contour maps of simulated evolving surface morphology, $h(x, y, t)$, of a coherently strained thin film starting with a surface morphology that consists of a periodic arrangement of nanopits, with the top view of one such nanopit structure shown in the unit cell of the regular nanopit pattern for a conical pit with a pit opening diameter $d_0$ of (a1-a5) 16 $l$, (b1-b5) 18 $l$, (c1-c5) 22 $l$, and (d1-d5) 28 $l$ at (a1, b1, c1, d1) $t = 0$, (a2, b2, c2, d2) $t = 0.6\,\tau$, (a3, b3, c3, d3) $t = 1.3\,\tau$, and (a4, b4, c4, d4) $t = 2.0\,\tau$. 3D views of the film surface morphology corresponding to the top views shown in (a4), (b4), (c4), and (d4) are depicted in (a5), (b5), (c5), and (d5), respectively. 1D surface profiles, $h(x; y, t)$, along the black solid lines marked on the 2D contour maps of (a1) and (a4), (b1) and (b4), (c1) and (c4), and (d1) and (d4) are plotted in blue and red, respectively, in (a6), (b6), (c6), and (d6), respectively. The 1D surface profiles plotted in red have been displaced upwards (along the $h$-axis) by 0.1 $l$ for clarity regarding their shapes. The other parameter values in the simulations are $d_{pit} = 60\,l$, $h_0 = 0.3\,l$, $h_p = 0.1\,l$, $k = 0.4\,l^{-1}$, and $\Xi_W = 0.0369$.

opening diameter smaller than a critical value will not cause the formation of a quantum dot (i.e., a single QD) inside the pit, as shown in Fig. 6(a6). However, in cases of pits with opening diameters slightly larger than the critical pit opening diameter, as in the configuration of Fig. 6(b1), the film surface morphological evolution will lead to formation of a single quantum dot inside the pit. Experimental studies have reached similar conclusions.[17]

In our simulation studies, we have been able to explore the surface morphological evolution of epitaxial films with conical pits that have opening diameters well beyond the range of $d_0$ that has been explored in experimental studies. Specifically, our simulations predict that employing patterns of pits with increasing pit opening diameter leads to formation of regular patterns of film surface features of increasing complexity such as single nanorings [Fig. 6(c5)], a central quantum dot surrounded by a single nanoring [Fig. 6(d5)], double concentric nanorings, a central quantum dot surrounded by double concentric nanorings, and so on, emerging from inside each pit. These nanostructures forming inside the pits are easily identified from the surface profiles on certain film cross sections in the heteroepitaxial configurations at the end of the first asymptotic state, such as the surface profiles shown in red in Figs. 6(a6), 6(b6), 6(c6), and 6(d6). The number of peaks in these profiles inside the surface pit, N, are characteristic of the features forming inside the pits: N = 0 means that there is no QD or other feature forming inside the pit, N = 1 indicates the formation of one quantum dot inside the pit, N = 2 indicates formation of a single nanoring inside the pit and surrounding its center, N = 3 means that a single quantum dot is formed at the central region of the pit surrounded by a nanoring centered at the pit's center, $N = 4$ means two concentric nanorings (or a double concentric nanoring) centered at the pit's center, and so on. For the parameters used in the simulations that yielded the representative results of Fig. 6, we have summarized the dependence of N on $d_0$ over the full range of $d_0$ examined in this study in the response diagram of Fig. 8(b). These results are discussed further, and the formation of the nanostructural features inside the pit is explained on the basis of a linear stability theory in Sec. IV.

### E. Effect of pit wall slope on film surface pattern

Figure 7 shows representative simulation results that capture the effect of varying the pit wall slope, controlled by setting the wave number $k$, on the resulting film surface nanopattern at the end of the first asymptotic state. Figures 7(a1)–7(a4), 7(b1)–7(b4), and 7(c1)–7(c4) show 2D contour maps of the evolving film surface morphology within the unit cell of a periodic pit pattern with the initial epitaxial film surface configurations shown in Figs. 7(a1), 7(b1), and 7(c1), respectively. In these initial heteroepitaxial configurations, we vary the wave number $k$ that determines the pit wall slope while keeping all the other design parameters constant. Figures 7(a4), 7(b4), and 7(c4) show the 2D contour maps of the epitaxial film surface configurations at the end of the first asymptotic state, with the 3D views of these configurations shown in Figs. 7(a5), 7(b5), and 7(c5), respectively. It is evident from these simulation results that varying the pit wall slope through varying the wave number $k$ has a major qualitative effect on the resulting nanopattern formation as can be seen in the surface profiles of Figs. 7(a6), 7(b6), and 7(c6). In our previous study,[26] we had shown that, in agreement with experimental reports,[17] the pit wall slope has to exceed a certain threshold for the formation of a quantum dot inside the pit, while all the other design parameters are kept constant.

In our simulation studies, we have explored the surface morphological evolution of epitaxial films with conical pits that have wall slopes, tuned by the wave number $k$, well beyond the range of pit wall slopes that has been explored experimentally. In particular, our simulations predict that increasing the pit wall slope in the employed pit patterns, through increasing the wave number $k$, leads to formation of increasingly complex regular patterns of film surface features

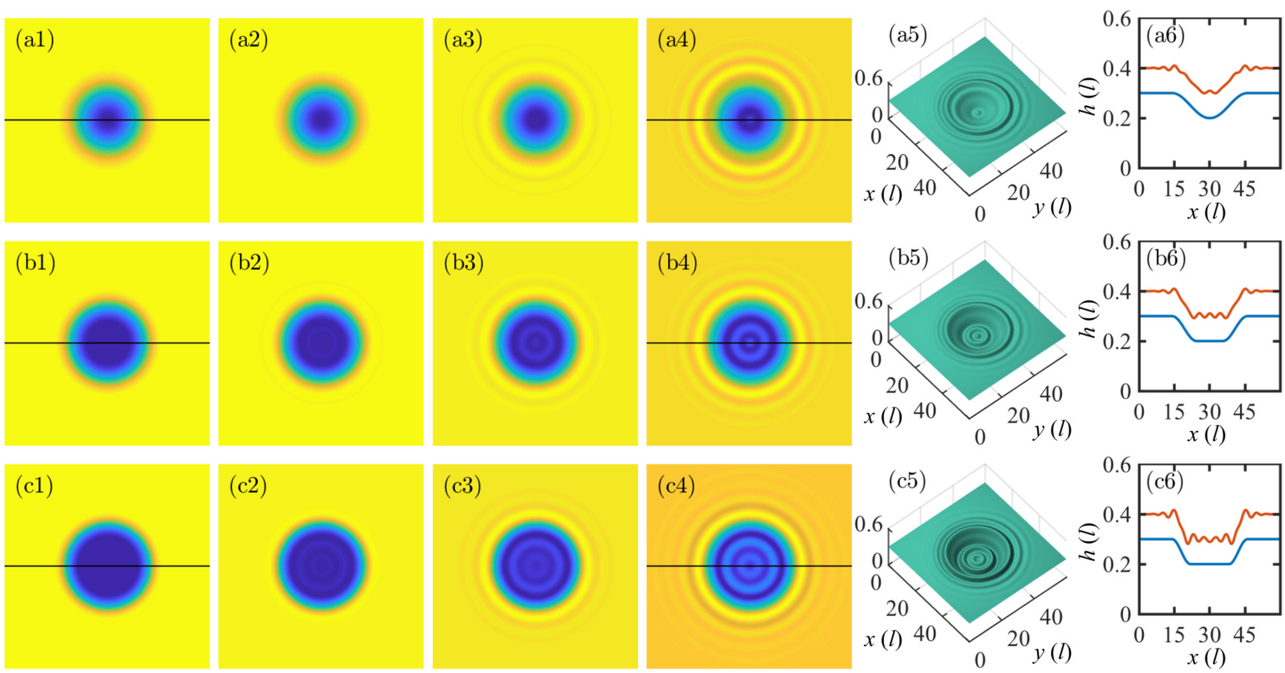


**FIG. 7.** (a)–(c) 2D contour maps of simulated evolving surface morphology, $h(x, y, t)$, of a coherently strained thin film starting with a surface morphology that consists of a periodic arrangement of nanopits, with the top view of one such nanopit structure shown in the unit cell of the regular nanopit pattern for (a1-a5) a conical pit with $k = 0.2\,l^{-1}$ at (a1) $t = 0$, (a2) $t = 0.8\,\tau$, (a3) $t = 1.7\,\tau$, and (a4) $t = 2.6\,\tau$; (b1-b5) a conical pit with $k = 0.3\,l^{-1}$ at (b1) $t = 0$, (b2) $t = 0.6\,\tau$, (b3) $t = 1.3\,\tau$, and (b4) $t = 2.0\,\tau$; and (c1-c5) a conical pit with $k = 0.4\,l^{-1}$ at (c1) $t = 0$, (c2) $t = 0.6\,\tau$, (c3) $t = 1.3\,\tau$, and (c4) $t = 2.0\,\tau$. 3D views of the film surface morphology corresponding to the top views shown in (a4), (b4), and (c4) are depicted in (a5), (b5), and (c5), respectively. 1D surface profiles, $h(x; y, t)$, along the black solid lines marked on the 2D contour maps of (a1) and (a4), (b1) and (b4), and (c1) and (c4) are plotted in blue and red, respectively, in (a6), (b6), and (c6), respectively. The 1D surface profiles plotted in red have been displaced upwards (along the $h$-axis) by $0.1\,l$ for clarity regarding their shapes. The other parameter values in the simulations are $d_{pit} = 60\,l$, $h_0 = 0.3\,l$, $h_p = 0.1\,l$, $d_0 = 32\,l$, and $\Xi_W = 0.0369$.

such as single nanorings, a single quantum dot at the pit's center surrounded by a single nanoring [Fig. 7(b5)], double concentric nanorings centered at the pit's center [Fig. 7(c5)], a central quantum dot surrounded by two concentric nanorings and so on, emerging from inside each pit. These nanostructural features forming inside the pits are again easily identified by inspecting the surface profiles in the heteroepitaxial configurations at the end of the first asymptotic state, such as the surface profiles shown in red in Figs. 7(a6), 7(b6), and 7(c6). For the parameters used in the simulations that yielded the representative results of Fig. 7, we have summarized the dependence on $k$ of the number of peaks N forming inside the pits and appearing in the surface profiles above in the response diagram of Fig. 8(c). Consistent with our discussion in Sec. III D, each value of N corresponds to a certain nanostructural feature forming inside the pit: if N is odd the feature consists of a central QD surrounded by $(N-1)/2$ concentric nanorings, while an even number N corresponds to formation of N/2 concentric nanorings centered at the pit's center without a central QD forming inside the pit. The formation of this complex sequence of nanostructural features, with N increasing with increasing $k$, emerging from inside the pit is explained on the basis of a linear stability theory in Sec. IV.

Figure 8(a) summarizes the film surface morphological response in a comprehensive response diagram for the dependence of the number of peaks N of the features emerging inside the surface pit on the two key design parameters, $d_0$ and $k$, which affect significantly the film surface pattern formation resulting from the evolution of the surface of the heteroepitaxial thin film until the end of the first asymptotic state. As mentioned above, in Figs. 8(b) and 8(c), N is plotted as a function of $d_0$ at constant $k$ and as a function of $k$ at constant $d_0$, respectively, with the value of the parameter that has been kept constant reported inside each plot. Figure 8(d) shows the dependence on the wave number $k$ that controls the pit wall slope of the critical pit opening diameter, $d_{0,c1}$, for the formation of a single quantum dot, i.e., the value of the pit opening diameter that marks the onset of the emergence of the $N = 1$ feature from inside the pit as a function of $k$.

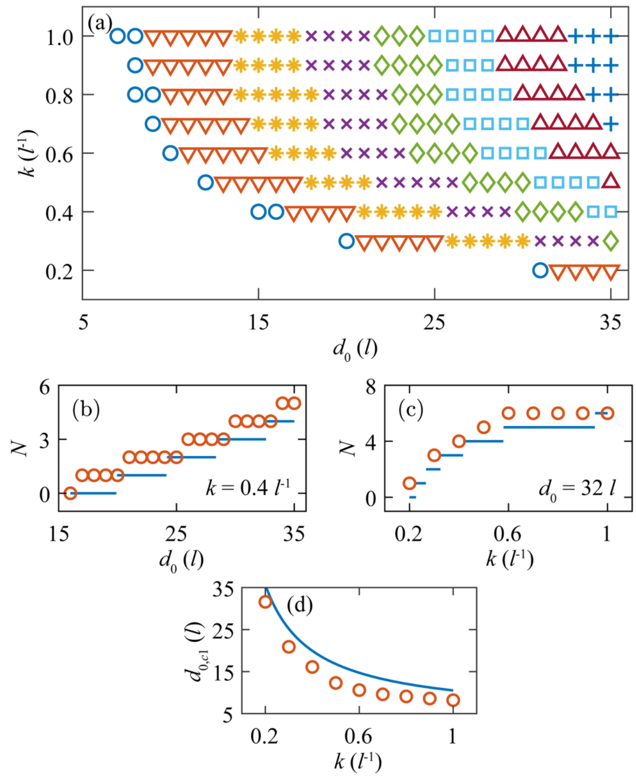


FIG. 8. (a) Number of peaks $N$ formed at the first asymptotic state inside the pits on the surface of a coherently strained thin film, starting with a surface morphology that consists of a periodic arrangement of conical nanopits, as a function of the pit opening diameter $d_0$ and the pit wall slope expressed by the wave number $k$. $N = 0$, 1, 2, 3, 4, 5, 6, and 7 are denoted by open circles, inverted open triangles, asterisks, crosses, open diamonds, open squares, open triangles, and plus symbols, respectively. Number of peaks $N$ formed at the first asymptotic state inside the pits on the film surface as a function of (b) pit opening diameter $d_0$ for a constant value of wave number $k = 0.4\,l^{-1}$ and (c) wave number $k$ for a constant value of pit opening diameter $d_0 = 32\,l$. (d) Dependence of the critical pit opening diameter $d_{0,c1}$ for the onset of formation of one quantum dot inside a pit on the pit wall slope expressed by the wave number $k$. In (b)–(d), solid lines and open circles denote predictions of linear stability theory and simulation results, respectively. The other parameter values used in the simulations and the linear stability analysis are $d_{pit} = 60\,l$, $h_0 = 0.3\,l$, $h_p = 0.1\,l$, and $\Xi_W = 0.0369$.

## IV. LINEAR STABILITY THEORY

We have explained the dependence of the number N of film surface features emerging inside the surface pit on the two parameters $d_0$ and $k$ in Figs. 8(b) and 8(c), respectively, and the dependence of $d_{0,c1}$ on $k$ in Fig. 8(d) based on a linear stability theory (LST) following the approach of Ref. 29. Specifically, to analyze the morphological stability of the planar film surface at the base of the pit under the action of the stress in the film due to the lattice mismatch strain, we use LST and follow the evolution of a nanopit's base flat surface upon perturbing its planar morphology with a low-amplitude plane-wave perturbation. The analysis of Ref. 29 gives the dispersion relation

$$\omega = 2\tilde{k}^3 - \tilde{k}^4 - \Xi_W \tilde{k}^2. \tag{3}$$

In Eq. (3), $\omega$ is the characteristic dimensionless rate of growth or decay of a perturbation with dimensionless wave number $\tilde{k}$, $\tilde{k} \equiv \sqrt{\tilde{k}_x^2 + \tilde{k}_y^2}$. The maximally unstable wave number $\tilde{k}_{max}$ corresponds to the maximum growth rate $\omega(\tilde{k}_{max}) > 0$ that will dominate the driven post-instability evolution of the planar surface of the pit's base. Consequently, LST implies that, for the confined conical pits under consideration, growth of the pit base surface perturbation at the dominant $\omega(\tilde{k}_{max})$ will lead to formation of features that correspond to concentric nanorings with or without the presence of a central quantum dot emerging from the center of the pit, with these features distributed uniformly over the base of the pit. Depending on the size of the pit's base, these nanoscale surface features can manifest themselves as a single central quantum dot ($N = 1$), a single nanoring ($N = 2$), a central quantum dot surrounded by a nanoring ($N = 3$), two concentric nanorings ($N = 4$), a central quantum dot surrounded by two concentric nanorings ($N = 5$), and so on, namely, axially symmetric features with the mode number N increasing (in a "radially outward" fashion) as the pit base increases. The maximally unstable (dimensional) wavelength, $\lambda_{\max} \equiv 2\pi/k_{\max} = 8\pi l/(3 + \sqrt{9 - 8\Xi_W})$, provides a length scale for the characteristic separation distance between consecutive nanorings emanating from the pit's base, and, thus, the number of peaks N observed inside the pit can be estimated (to within the linear stability approximations) by $N = [d_p/\lambda_{\max}]$, where $d_p$ is the diameter of the circular disc that constitutes the base of the "conical" pit and the square brackets are used to denote the integer part of the bracketed quantity. The results of the linear stability theory are plotted as blue lines (or line segments) in Figs. 8(b)–8(d) and are in very good agreement with the (fully nonlinear) simulation predictions. Moreover, the LST predictions provide a comprehensive explanation and analytical support for the numerical simulation results and constitute an efficient design tool for fabricating pit patterns that will result in certain regular nanopatterns on the film surface, consisting of certain types of features (mode N) with controlled dimensions (wavelength $\lambda_{\max}$).

## V. SUMMARY AND CONCLUSIONS

In summary, we have carried out a comprehensive computational analysis of complex nanostructure formation on the surface of coherently strained thin films grown epitaxially on pit-patterned substrates based on self-consistent dynamical simulations according to an experimentally validated film surface evolution model. We focused on conical pit patterns and investigated systematically the effects on the resulting film surface nanopattern of varying the key geometrical pit pattern design parameters, namely, the film thickness, pit-pattern period, pit depth, pit opening diameter, and pit wall inclination. We found the pit opening diameter and the pit wall slope to be the most significant design parameters and that their variation can cause formation of complex nanostructures inside the pits of a regular pit pattern on the epitaxial film surface, which include quantum dots, as well as single nanorings and multiple concentric nanorings with or without a central quantum dot inside each pit. Our computational findings are supported by linear stability theory that explains the nanostructural features forming inside the pits as the outcome of a Stranski-Krastanow instability.

Although our model has been validated for the Ge/Si heteroepitaxial system, it can be parameterized properly for any heteroepitaxial film/substrate material system and extended to multicomponent (as opposed to elemental material) films. Computer simulations based on such models can be used to develop growth strategies and guide the design of systematic experimental protocols toward fabrication of ordered nanostructure patterns on epitaxial film surfaces, including patterns of complex nanostructures with controlled geometries and dimensions. Furthermore, although the present study focused on pit patterns consisting of conical pits, other pit geometries, such as pyramidal pits, merit analogous systematic investigation and exploration of the ordered nanostructure patterns that can be formed as a result of film surface morphological response for films grown epitaxially on such patterned substrates. Such computational studies are currently underway and will be presented in a forthcoming publication.

## ACKNOWLEDGMENTS

This work was supported by the U.S. Department of Energy (DOE), Office of Basic Energy Sciences, Division of Materials Sciences and Engineering (Award No. DE-FG02-07ER46407).

## REFERENCES

[1]E. Yablonovitch, Phys. Rev. Lett. **58**, 2059 (1987).
[2]S. K. O'Leary, B. E. Foutz, M. S. Shur, and L. F. Eastman, Appl. Phys. Lett. **88**, 152113 (2006).
[3]G. Xu, Y. J. Ding, H. Zhao, G. Liu, M. Jamil, N. Tansu, I. B. Zotova, C. E. Stutz, D. E. Diggs, N. Fernelius, F. K. Hopkins, C. S. Gallinat, G. Koblmüller, and J. S. Speck, Semicond. Sci. Technol. **25**, 015004 (2010).
[4]G. D. Metcalfe, H. Shen, M. Wraback, G. Koblmüller, C. Gallinat, F. Wu, and J. S. Speck, Appl. Phys. Express **3**, 092201 (2010).
[5]Z. Yue, F. Lisdat, W. J. Parak, S. G. Hickey, L. Tu, N. Sabir, D. Dorfs, and N. C. Bigall, ACS Appl. Mater. Interfaces **5**, 2800 (2013).
[6]J. M. Costa-Fernández, R. Pereiro, and A. Sanz-Medel, Trend Anal. Chem. **25**, 207 (2006).
[7]S. Y. Chou, M. S. Wei, P. R. Krauss, and P. B. Fischer, J. Appl. Phys. **76**, 6673 (1994).
[8]D. J. Eaglesham and M. Cerullo, Phys. Rev. Lett. **64**, 1943 (1990).
[9]F. M. Ross, J. Tersoff, and R. M. Tromp, Phys. Rev. Lett. **80**, 984 (1998).
[10]M. K. Yakes, C. D. Cress, J. G. Tischler, and A. S. Bracker, ACS Nano **4**, 3877 (2010).
[11]J. Lee, Z. M. Wang, N. Strom, Y. I. Mazur, and G. Salamo, Appl. Phys. Lett. **89**, 202101 (2006).
[12]P. S. Wong, G. Balakrishnan, N. Nuntawong, J. Tatebayashi, and D. L. Huffaker, Appl. Phys. Lett. **90**, 183103 (2007).
[13]O. G. Schmidt, C. Deneke, S. Kiravittaya, R. Songmuang, H. Heidemeyer, Y. Nakamura, R. Zapf-Gottwick, C. Muller, and N. Y. Jin-Phillipp, IEEE J. Sel. Top. Quant. **8**, 1025 (2002).
[14]L. Wang, A. Rastelli, S. Kiravittaya, P. Atkinson, F. Ding, C. C. B. Bufon, C. Hermannstädter, M. Witzany, G. J. Beirne, P. Michler, and O. G. Schmidt, New J. Phys. **10**, 045010 (2008).
[15]M. Grydlik, M. Brehm, and F. Schäffler, Nanoscale Res. Lett. **7**, 601 (2012).
[16]M. Brehm, M. Grydlik, T. Tayagaki, G. Langer, F. Schäffler, and O. G. Schmidt, Nanotechnology **26**, 225202 (2015).
[17]M. Grydlik, G. Langer, T. Fromherz, F. Schäffler, and M. Brehm, Nanotechnology **24**, 105601 (2013).
[18]C.-T. Kuo, L.-H. Hsu, Y.-Y. Lai, S.-Y. Cheng, H.-C. Kuo, C.-C. Lin, and Y.-J. Cheng, Appl. Surf. Sci. **405**, 449 (2017).
[19]S. Kiravittaya, A. Rastelli, and O. G. Schmidt, Rep. Prog. Phys. **72**, 046502 (2009).
[20]S. S. Sarkar, A. K. Katiyar, A. Sarkar, A. Dhar, A. Rudra, R. K. Khatri, and S. K. Ray, Appl. Surf. Sci. **437**, 144 (2018).
[21]M. Salvalaglio, R. Backofen, A. Voigt, and F. Montalenti, Nanoscale Res. Lett. **12**, 554 (2017).
[22]J.-N. Aqua and X. Xu, Surf. Sci. **639**, 20 (2015).
[23]J.-N. Aqua and X. Xu, Phys. Rev. E **90**, 030402 (2014).

[24]H. Hu, H. J. Gao, and F. Liu, Phys. Rev. Lett. **101**, 216102 (2008).
[25]A. Pascale, I. Berbezier, A. Ronda, and P. C. Kelires, Phys. Rev. B **77**, 075311 (2008).
[26]A. Kumar, L. Du, and D. Maroudas, Mater. Res. Express **5**, 086303 (2018).
[27]B. J. Spencer, Phys. Rev. B **59**, 2011 (1999).
[28]Y. Pang and R. Huang, Phys. Rev. B **74**, 075413 (2006).
[29]L. Du and D. Maroudas, Appl. Phys. Lett. **109**, 023103 (2016).
[30]G. Tegze, G. Bansel, G. I. Tóth, T. Pusztai, Z. Fan, and L. Gránásy, J. Comput. Phys. **228**, 1612 (2009).
[31]F. K. LeGoues, M. Copel, and R. Tromp, Phys. Rev. Lett. **63**, 1826 (1989).
[32]A. A. Williams, J. M. C. Thornton, J. E. Macdonald, R. G. van Silfhout, J. F. van der Veen, M. S. Finney, A. D. Johnson, and C. Norris, Phys. Rev. B **43**, 5001 (1991).
[33]L. Du and D. Maroudas, Appl. Phys. Lett. **110**, 103103 (2017).
[34]L. Du and D. Maroudas, J. Appl. Phys. **124**, 125302 (2018).
[35]L. Du, M. Khenner, and D. Maroudas, Phys. Rev. Mater. **2**, 083403 (2018).